nature physics

SUPPLEMENTARY INFORMATION
https://doi.org/10.1038/s41567-018-0150-8

In the format provided by the authors and unedited.

# Topological kinematics of origami metamaterials

**Bin Liu[1,2,8]*, Jesse L. Silverberg[1,3,4,8], Arthur A. Evans[5], Christian D. Santangelo[5], Robert J. Lang[6], Thomas C. Hull[7] and Itai Cohen[1]**

[1]Department of Physics, Cornell University, Ithaca, NY, USA. [2]School of Natural Sciences, University of California, Merced, Merced, CA, USA. [3]Wyss Institute for Biologically Inspired Engineering, Harvard University, Boston, MA, USA. [4]Department of Systems Biology, Harvard Medical School, Boston, MA, USA. [5]Department of Physics, University of Massachusetts Amherst, Amherst, MA, USA. [6]Lang Origami, Alamo, CA, USA. [7]Department of Mathematics, Western New England University, Springfield, MA, USA. [8]These authors contributed equally: Bin Liu, Jesse L. Silverberg.
*e-mail: bliu27@ucmerced.edu

# Supplementary Information: Toplogical kinematics of origami metamaterials

Bin Liu,[1,2] Jesse L. Silverberg,[1,3,4] Arthur A. Evans,[5] Christian D. Santangelo,[5] Robert J. Lang,[6] Thomas C. Hull,[7] and Itai Cohen[1]

[1]*Department of Physics, Cornell University, Ithaca, NY 14850*
[2]*School of Natural Sciences, University of California, Merced, Merced, CA 95343, USA*
[3]*Wyss Institute for Biologically Inspired Engineering, Harvard University, Boston, MA 02115, USA*
[4]*Department of Systems Biology, Harvard Medical School, Boston, MA 02115, USA*
[5]*Department of Physics, University of Massachusetts Amherst, Amherst, Massachusetts 01003, USA*
[6]*Lang Origami, Alamo, California 94507*
[7]*Department of Mathematics, Western New England University, Springfield, MA 01119, USA*

(Dated: March 28, 2018)

## SYMBOLIC MODEL OF A DEGREE-6 VERTEX

We model the degree-6 Miura-ori vertex as in Figure S1(a). The crease pattern is determined by 6 neighboring vertices on a circle, here $\mathbf{v}_1$, $\mathbf{v}_2$, $\cdots$, $\mathbf{v}_6$, and the radius has 1 unit length. We denote by $t_1$, $t_2$, and $t_3$ the *folding angles* (i.e., $\pi-$ the dihedral angle) of the creases $\mathbf{v}_1$, $\mathbf{v}_2$, and $\mathbf{v}_3$ respectively. Here $t_2$ is assigned to be a mountain fold, i.e. $t_2 < 0$, while $t_1$ and $t_3$ are virtual folds, corresponding to facet bending for a degree-4 vertex [S1]. If we fix the location of the sector between creases $\mathbf{v}_1$ and $\mathbf{v}_6$, we can determine $\mathbf{v}_4'$, the final position of the crease $\mathbf{v}_4$ after sequentially folding along $\mathbf{v}_3$, $\mathbf{v}_2$ and $\mathbf{v}_1$, using standard kinematics:

$$\mathbf{v}_4' = R_z\left(-\frac{3(\pi-\alpha)}{2}\right) R_x(-t_1) R_z\left(\frac{3(\pi-\alpha)}{2}\right) R_z(-(\pi-\alpha)) R_x(-t_2) R_z(\pi-\alpha) R_z\left(-\frac{\pi-\alpha}{2}\right) R_x(-t_3) R_z\left(\frac{\pi-\alpha}{2}\right) \cdot \mathbf{v}_4$$

where $R_x(\theta)$ and $R_z(\theta)$ denote the $3\times 3$ rotation matrices about the $x$- and $z$-axes, respectively, with $\theta$ the angle of rotation.

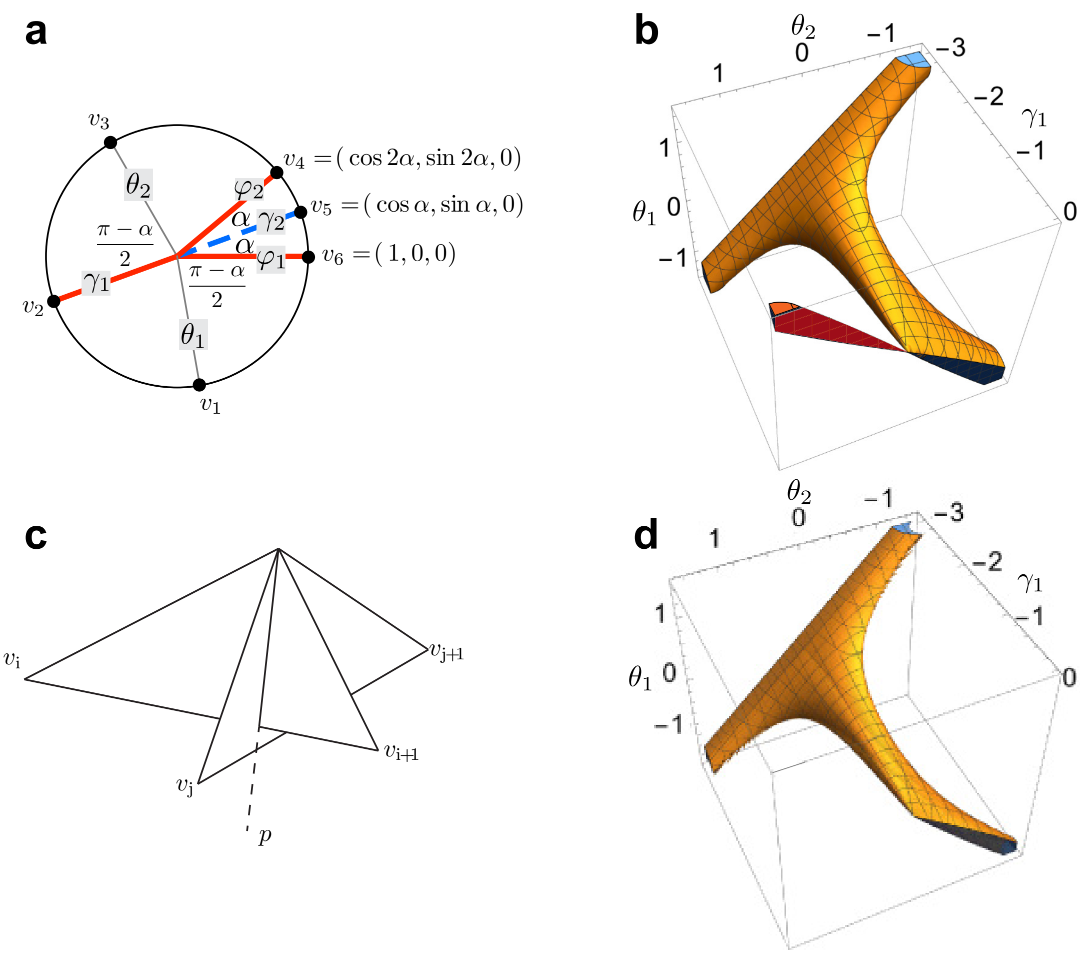


FIG. S1. A symbolic model of the degree-6 Miura-ori vertex is constructed. (a) The vertex coordinates are given. The rigid folding process is then modeled using standard kinematic techniques. The mountain and valley folds are shown in solid and dashed thick lines, and thin gray lines denote the virtual creases, which correspond to facet bending in a degree-4 vertex [S1]. (b) The configuration space when $\alpha = 0.16$ rad. We let the $\theta_1$, $\gamma_1$, and $\theta_2$ be the *folding angles* of the creases $\mathbf{v}_1$, $\mathbf{v}_2$, and $\mathbf{v}_3$ respectively. The topological separable region in red corresponds to pop-through defects. (c) An example of intersection between two facets. (d) A modified configuration space that eliminates self-intersections, pop-through defects, incorrect assignment of mountain or valley configurations for $\mathbf{v}_2$, $\mathbf{v}_4$, $\mathbf{v}_5$, and $\mathbf{v}_6$.

## CONFIGURATION SPACE

The greatest distance the points $\mathbf{v}_4$ and $\mathbf{v}_6$ can be from each other is in the unfolded state, where $||\mathbf{v}_4 - \mathbf{v}_6|| = 2|\sin\alpha|$. We then obtain the configuration space for the folded vertex by plotting all points $(t_1, t_2, t_3)$ that satisfy the inequality

$$||\mathbf{v}'_4 - \mathbf{v}_6|| \leq 2|\sin\alpha|.$$

This configuration space when $\alpha = 0.16$ is shown in Figure S1(b). The singular point $(0, 0, 0)$ in the configuration space corresponds to the unfolded state.

Potential self-intersection of the single vertex can be further excluded from the accessible configuration space by satisfying the following criteria. For any pair of facets $i$ and $j$, comprising $\mathbf{v}_i$, $\mathbf{v}_{i+1}$, $\mathbf{v}_j$, and $\mathbf{v}_{j+1}$, the intersection-free condition requires (see Fig. S1(c))

$$(\mathbf{v}_i \times \mathbf{p}) \cdot (\mathbf{v}_{i+1} \times \mathbf{p}) > 0, \text{ or } (\mathbf{v}_j \times \mathbf{p}) \cdot (\mathbf{v}_{j+1} \times \mathbf{p}) > 0,$$

where $\mathbf{p}$ is the intersection line between two infinite planes containing this pair of facets.

$$\mathbf{p} = (\mathbf{v}_i \times \mathbf{v}_{i+1}) \times (\mathbf{v}_j \times \mathbf{v}_{j+1}).$$

To ensure that $\mathbf{v}_4$ and $\mathbf{v}_6$ correspond to two mountain folds, we have the two following equalities

$$[(\mathbf{v}_5 \times \mathbf{v}_4) \times (\mathbf{v}_4 \times \mathbf{v}_3)] \cdot \mathbf{v}_4 \leq 0 \text{ and } [(\mathbf{v}_1 \times \mathbf{v}_6) \times (\mathbf{v}_6 \times \mathbf{v}_5)] \cdot \mathbf{v}_1 \leq 0.$$

Misfolds associated with a swap between mountain and valley vertices (and vice versa) can be excluded explicitly by the following criterion,

$$[(\mathbf{v}_4 \times \mathbf{v}_2) \times (\mathbf{v}_2 \times \mathbf{v}_6)] \cdot \mathbf{v}_5 \geq 0.$$

The resulting configuration space satisfying all above criteria are shown in Fig. S1(d).

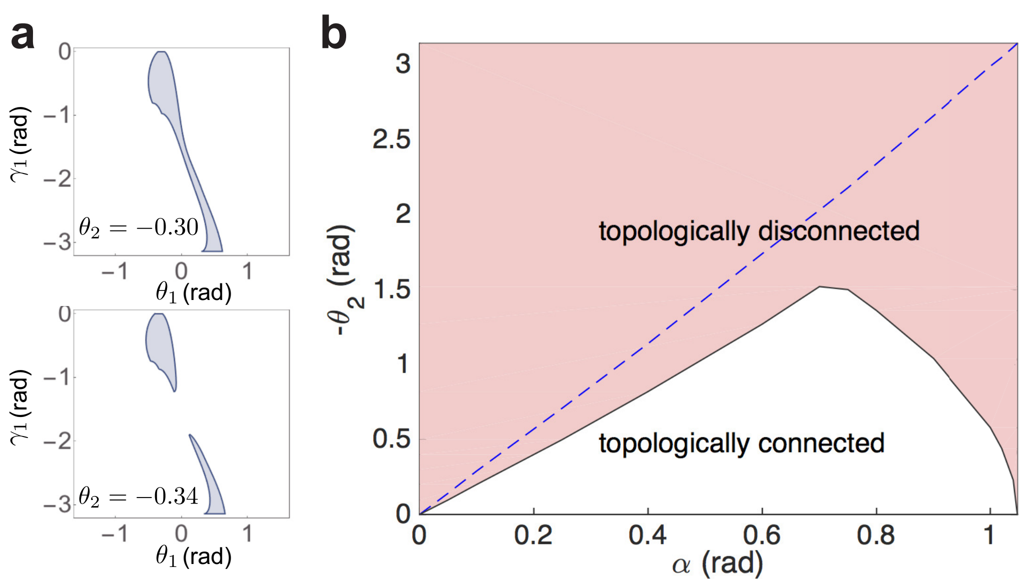


FIG. S2. Restricted configuration spaces due to fold angle $\theta_2$. (a) For plane angle $\alpha = 0.16$ rad (Fig. S1), given fold angles $\theta_2$ lead to either simply connected ($\theta_2 = -0.3$ rad) or disconnected ($\theta_2 = -0.34$ rad) configuration subspaces. (b) The critical $\theta_2$, above which the configuration subspaces is disconnected (shaded) is shown as a function of the plane angle $\alpha$. The dashed line shows the critical $\theta_2$ without considering self-intersections.

Given a fold angle along one crease will restrict the 3-D configuration space into a 2-D subspace. An example of such subspaces (for plane angle $\alpha = 0.16$ rad) is shown in Fig. S2(a). By increasing the magnitude of fold angle $\theta_2$ above a critical value $\theta_{2,c} \approx -0.32$ rad, the configuration space topology varies from one simply connected region to two disconnected regions. Such critical fold angles $\theta_{2,c}$ as a function of $\alpha$ are shown in Fig. S2(b).

## RECONSTRUCTION OF THE ORIGAMI MORPHOLOGY

3D reconstructions of the origami structure are obtained by matching the 2D coordinates of all its vertices with a projection of an idealized origami model. The crease length of the origami model is determined by the crease pattern. For any two vertices $\mathbf{r}_i$ and $\mathbf{r}_j$ that are connected by a single crease of length $l_{ij}$, they must satisfy the following condition

$$r_{ij} = |\mathbf{r}_{ij}| = |\mathbf{r}_i - \mathbf{r}_j| = l_{ij}. \tag{S1}$$

The corresponding vertex coordinates $(X_i,\, Y_i)$ in the real origami structure are obtained from its top-view images, using MATLAB's camera calibration toolbox to correct for distortions. The location of the vertices are initially identified by manually tracking the vertex positions. Using MATLAB's feature tracking algorithm in conjunction with particle image velocimetry [S2] we automatically track the vertex locations in successive images. To calculate the out-of-plane coordinates of these vertices along $z$, we draw inspiration from previous work [S3] and minimize the penalty function:

$$V(\{\mathbf{r}_i\}) = \frac{k_1}{2}\sum_i \left[(x_i - g(z_i)X_i)^2 + (y_i - g(z_i)Y_i)^2\right] + \frac{k_2}{2}{\sum_{i>j}}'(r_{ij} - l_{ij})^2, \tag{S2}$$

where $k_1 \ll k_2$ are the effective spring constants that constrain these vertices, $g(z) = 1 - z/H$ is the first-order perspective correction for a camera placed at $(0, 0, H)$, and $|z/H| \ll 1$ [S4]. Here, $\sum'$ denotes the summation over directly connected vertices. The minimal value $\min V(\{\mathbf{r}_i\})$ can be achieved iteratively using a conjugate gradient method. At the $(k+1)$th iteration with a step size $\Delta$, we have

$$\frac{\mathbf{r}_i^{(k+1)} - \mathbf{r}_i^{(k)}}{\Delta} = k_1\left[\left(g\left(z_i^{(k)}\right)X_i - x_i^{(k)}\right)\hat{x} + \left(g\left(z_i^{(k)}\right)Y_i - y_i^{(k)}\right)\hat{y}\right] + k_2{\sum_j}'\left(l_{ij} - r_{ij}^{(k)}\right)\hat{\mathbf{r}}_{ij}^{(k)}. \tag{S3}$$

The initial coordinates are set as $x_i^{(0)} = X_i$, $y_i^{(0)} = Y_i$, and $z_i^{(0)}$ slightly off from 0 with its sign determined by the mountain-valley assignments. The convergence is achieved at a tolerance level $\delta$ so that $\sqrt{{\sum_{i>j}}'(r_{ij} - l_{ij})^2} < \delta$. The value of $\delta$ is typically set at $10^{-10}$ for relatively low computational time. In addition to the 3D morphology, the obtained coordinates also allow us to compute the folding angles for each vertex.

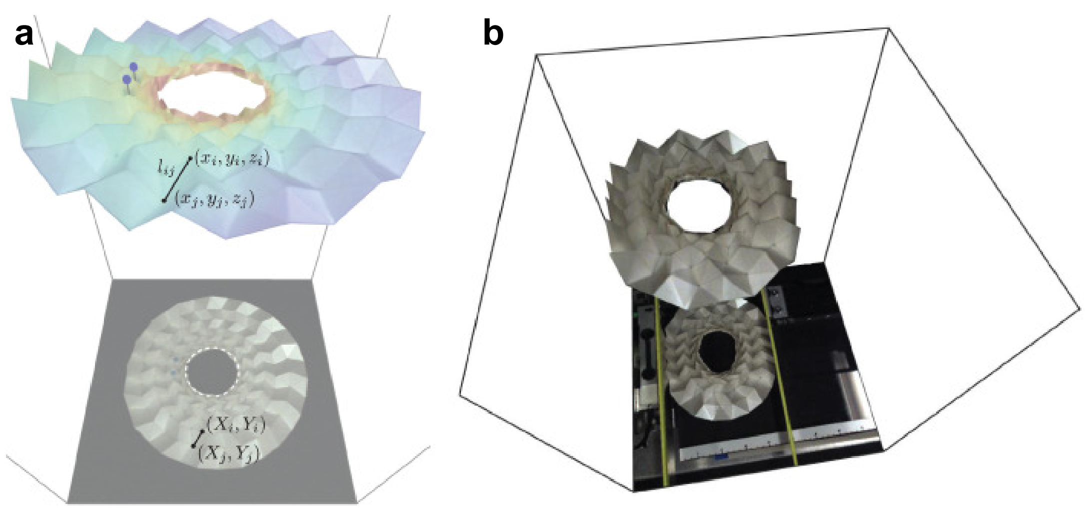


FIG. S3. 3D reconstruction of the origami structure. (a) Schematics of the reconstruction, where $(X, Y)$ are the 2D coordinates from the raw image and $(x, y, z)$ are the 3D coordinates reconstructed by constraining these vertices with a given crease length $l$. (b) An example of this 3D reconstruction showing the deformation of the origami structure under compression, achieved by tracing the 2D coordinates $(X, Y)$ of all the vertices.

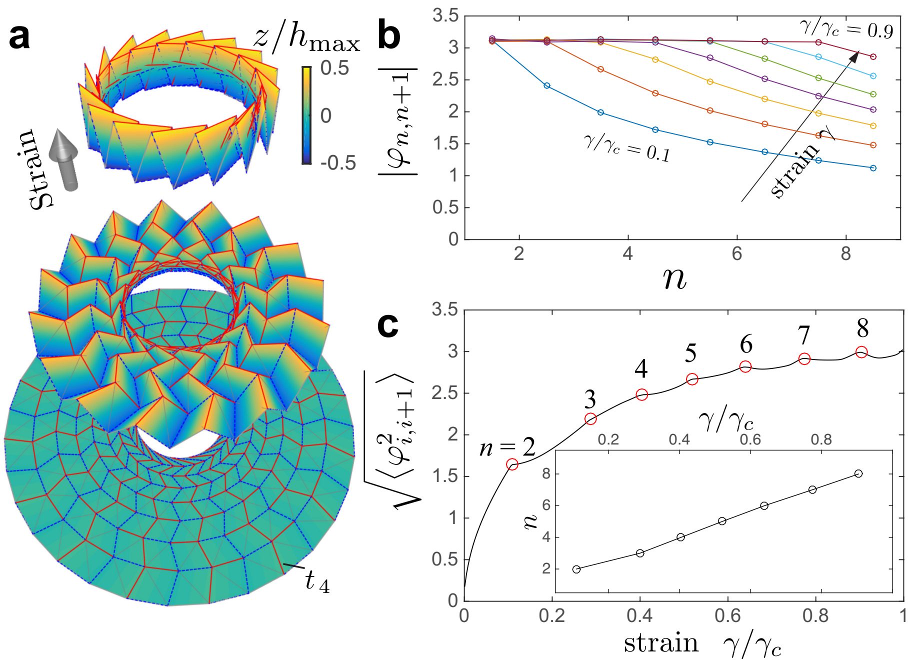


FIG. S4. Simulation of the folding kinematics of a Miura-ori ring structure. (a) Under isotropic strain, the origami structure deforms from a plane sheet (bottom) and collapses onto a cylindrical shape (top). (b) Folding angle $\varphi_{i,i+1}$ for creases shared by adjacent vertices versus vertex layer number $n$ at different values of compressive strain $\gamma/\gamma_c$. Here, $\gamma_c$ is the maximum strain that can be applied without buckling the inner boundary. Generally, we observe the outer creases to have a lower value of $\varphi_{i,i+1}$. As strain increases this value rapidly approaches the saturation angle of $\pi$. (c) The root mean square of $\varphi_{i,i+1}$ for all vertices versus strain $\gamma/\gamma_c$. The abrupt changes in the slope are associated with the snapping behavior of the folded sheet. We identify these locations by taking the second-order derivative, identifying the local minima, and labeling them with the number of collapsed layers of vertices. The number of collapsed layers $n$ versus the strain $\gamma/\gamma_c$ is shown in the inset.

## NUMERICAL SIMULATION OF THE FOLDED STRUCTURE

The folded origami structure can be simulated numerically with a similar scheme for the penalty function. Instead of matching the 2D projection of the position of every vertex, we restricted the coordinates of a subset of all $N$ vertices on the outer boundary and obtain the optimized origami structure. The penalty function thus becomes

$$V(\{\mathbf{r}_i\}) = \frac{k_1}{2}\sum_i{}'' \left[(x_i - X_i)^2 + (y_i - Y_i)^2\right] + \frac{k_2}{2}\sum_{i>j}{}'(r_{ij} - l_{ij})^2 + \frac{k_3 L^2}{2}\sum_\sigma t_\sigma^2, \tag{S4}$$

where $\sum_i{}''$ is performed over the restricted vertices, $t_\sigma$'s are the folding angle along the virtual creases, $k_3$ is the bending stiffness of the virtual creases, and $L$ is the size of the unfolded sheet. The non-vanishing bending stiffness $k_3$ leads to a unique folded structure associated with the lowest bending energy for all virtual creases. It should be noted that the penalty function here does not forbid any self-intersections.

In case of isotropic compression of the Miura-ori ring, the radius of the vertices on the outer boundaries are prescribed as $\sqrt{X^2 + Y^2} = (1-\gamma)R_0$, where $\gamma$ is the compressive strain, and $R_0$ is the radius of the unfolded origami sheet. The penalty function can be rewritten as

$$V(\{\mathbf{r}_i\}) = \frac{k_1}{2}\sum_i{}'' \left(\sqrt{x_i^2 + y_i^2} - (1-\gamma)R_0\right)^2 + \frac{k_2}{2}\sum_{i>j}{}'(r_{ij} - l_{ij})^2 + 2k_3 R_0^2\sum_\sigma t_\sigma^2, \tag{S5}$$

The folding kinematics can be solved as

$$\frac{\mathbf{x_i}^{(k+1)} - \mathbf{x_i}^{(k)}}{\Delta} = \tag{S6}$$

$$\begin{cases} -k_1 \left( x_i^{(k)} \hat{x} + y_i^{(k)} \hat{y} \right) \left( 1 - \frac{(1-\gamma) R_0}{\sqrt{x_i^{(k)\,2} + y_i^{(k)\,2}}} \right) - k_2 {\sum_j}' \left( r_{ij}^{(k)} - l_{ij} \right) \hat{\mathbf{r}}_{ij}^{(k)} - 4 k_3 R_0^2 \sum_\sigma \hat{\theta}_{i\sigma}^{(k)} t_\sigma^{(k)}, \\ \quad \text{for } i \in \text{outer boundary}, \\ -k_2 {\sum_j}' \left( r_{ij}^{(k)} - l_{ij} \right) \hat{\mathbf{r}}_{ij}^{(k)} - 4 k_3 R_0^2 \sum_\sigma \hat{\theta}_{i\sigma}^{(k)} t_\sigma^{(k)}, \text{ otherwise.} \end{cases} \tag{S7}$$

Here, $\hat{\theta}_{i\sigma} = \hat{d}_\sigma \times (\mathbf{r}_i - \mathbf{v}_\sigma) / \left| \hat{d}_\sigma \times (\mathbf{r}_i - \mathbf{v}_\sigma) \right|$ with $\hat{d}_\sigma$ and $\mathbf{v}_\sigma$ are the orientation and center of the virtual crease $\sigma$. In practice, we let $k_1\Delta = 0.1$, and $k_2\Delta = k_3\Delta = 0.005$. Using the Runge-Kutta method, the differential equation leads to convergent coordinates of all vertices. An example of such simulated folding is shown and described in Fig. S4.

## EXPERIMENTAL CHARACTERIZATION OF THE SEQUENTIAL BISTABILITY

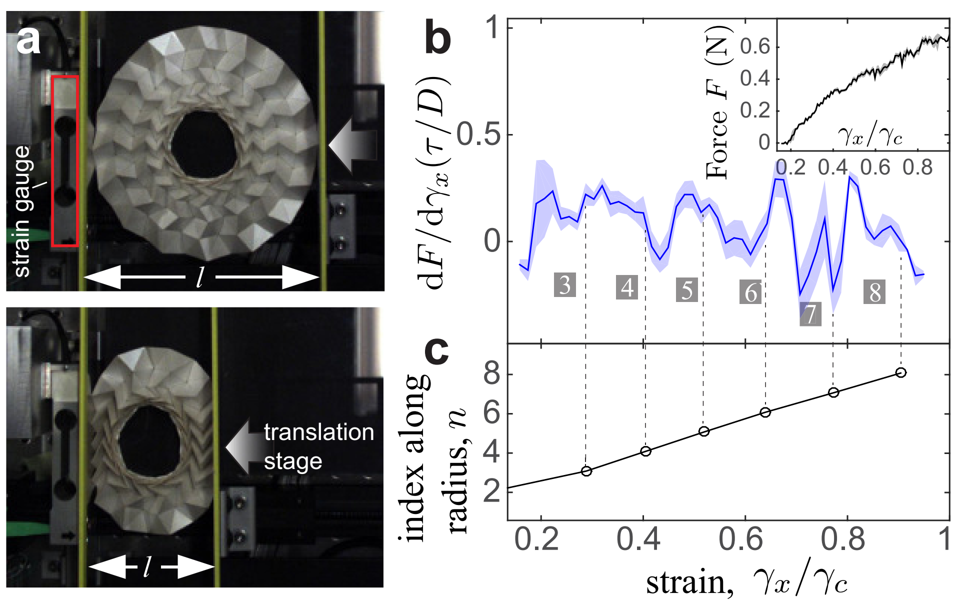


FIG. S5. Realization of sequential bistability through vertex-vertex coupling. (a) The Miura-ori ring is deformed uni-axially between two parallel plates. (b) The compressive modulus of the Miura-ori ring $K \propto \frac{dF}{d\gamma_x}$ is obtained from the force-strain relationship $F$ vs. $\gamma_x/\gamma_c$. Here $\gamma_c = 0.75$ and corresponds to the strain at which the entire sheet snaps into a cylindrical wall. The modulus $K = \frac{dF}{d\gamma_x} \cdot (\tau/D)$, normalized by flexural rigidity $D$ and thickness of the sheet $\tau$, shows a sequence of drops in its value each of which corresponds to a snap. For both the force and the modulus curves, the solid line is a 10-point boxcar average of the measured value and the shaded band is the 10-point boxcar standard deviation. (c) We simulated uniform compression of this structure and overlay the normalized strain values at which each layer undergoes a snapping transition (circles). The dashed lines are guides to the eye.

To characterize the topologically disconnected configurations in a Miura-ori ring, we laterally compressed the fabricated structure between two plates (Fig. S5(a)). We find that the structure is able to accommodate a large degree of compressive strain $\gamma_x = (l_0 - l)/l_0$, where $l_0$ and $l$ correspond to the lateral size of the unfolded and folded sheet respectively. During compression, the innermost layer is the first to collapse. Upon further compression, successive layers collapse onto the inner layer (Supplementary Movie 2). At the same time the remaining uncollapsed layers retain their flexibility. Importantly, throughout the entire folding process up to where the strain reaches $\gamma_c$ indicating full collapse, the inner boundary maintains its shape indicating effective strain isolation.

The snapping behavior of successive layers can be quantified by the compressive modulus, which is the derivative of the applied compressive force $F$ with respect to the strain $\gamma_x$ (Fig. S5(b)). We find that each snap, indicated by the number of collapsed layers $n$, corresponds to a rapid decrease of $dF/d\gamma_x$ as the normalized strain $\gamma_x/\gamma_c$ is increased

(Fig. S5(b)). This decrease arises from the extra space that is released when a layer snaps into place, which relaxes the folds in the remaining layers and reduces their resistance to compression.

To determine the theoretical strain value associated with successive snapping of layers onto the inner cylinder, we simulate an isotropic deformation of the same origami geometry (Fig. S4(c)). We plot the number of collapsed layers as a function of the applied normalized strain (black line and open circles in Fig. S5(c)). We find that comparison with $dF/d\gamma_x$ (vertical dashed lines) identifies where the structure undergoes an abrupt drop in compressive modulus due to each sequential snap (labeled by $n$).


[S1] Z. Y. Wei, Z. V. Guo, L. Dudte, H. Y. Liang, and L. Mahadevan, Phys. Rev. Lett. **110** (2013).

[S2] J. Westerweel, "Digital particle image velocimetry: theory and application," Delft University Press (1993).

[S3] A. Smith, A. E. Smith, D. W. Coit, T. Baeck, and D. Fogel, in *Handbook of Evolutionary Computation*, edited by T. Baeck, D. Fogel, and Z. Michalewicz (Institute of Physics Publishing and Oxford University Press, 1997).

[S4] I. Carlbom and J. Paciorek, ACM Computing Surveys (CSUR) **10**, 465 (1978).